

Non-local Meets Global: An Integrated Paradigm for Hyperspectral Denoising

Wei He
RIKEN AIP
wei.he@riken.jp

Quanming Yao
4Paradigm
qyaoaa@connect.ust.hk

Chao Li
RIKEN AIP
Chao.Li@riken.jp

Naoto Yokoya
RIKEN AIP
naoto.yokoya@riken.jp

Qibin Zhao
RIKEN AIP
qibin.Zhao@riken.jp

Abstract

Non-local low-rank tensor approximation has been developed as a state-of-the-art method for hyperspectral image (HSI) denoising. Unfortunately, with more spectral bands for HSI, while the running time of these methods significantly increases, their denoising performance benefits little. In this paper, we claim that the HSI underlines a global spectral low-rank subspace, and the spectral subspaces of each full band patch groups should underlie this global low-rank subspace. This motivates us to propose a unified spatial-spectral paradigm for HSI denoising. As the new model is hard to optimize, we further propose an efficient algorithm for optimization, which is motivated by alternating minimization. This is done by first learning a low-dimensional projection and the related reduced image from the noisy HSI. Then, the non-local low-rank denoising and iterative regularization are developed to refine the reduced image and projection, respectively. Finally, experiments on synthetic and both real datasets demonstrate the superiority against the other state-of-the-arts HSI denoising methods.

1. Introduction

Recent decades have witnessed the development of hyperspectral imaging techniques [4, 38, 18]. The hyperspectral imaging system is able to cover the wavelength region from 0.4 to $2.5\mu\text{m}$ at a nominal spectral resolution of 10 nm. With the wealth of available spectral information, hyperspectral images (HSI) have the high spectral diagnosis ability to distinguish precise details even between the similar materials [2, 31], providing the potential advantages of application in remote sensing [32, 33], medical diagnosis [20], face recognition [27, 33], quality control [17] and so on. Due to instrumental noise, HSI is often corrupted by Gaussian noise, which significantly influences the subsequent applications. As a preprocessing, HSI denoising is

a fundamental step prior to HSI exploitation [6, 41, 43].

For HSI denoising, the spatial non-local similarity and global spectral correlation are the most two important properties. The spatial non-local similarity suggests that similar patches inside a HSI can be grouped and denoised together. The related methods [9, 12, 13, 28, 36, 45] denoise the HSIs via group matching of *full band patches* (FBPs, stacked by patches at the same location of HSI over all bands) and low-rank denoising of each non-local FBP group (NLFBPG). These methods have achieved state-of-the-art performance. However, they still face a crucial problem. For HSIs, the higher spectral dimension means the higher discriminant ability [2], thus more spectrums are desired. As the spectral number increases, the size of NLFBPG also becomes larger, leading to significantly more computations for the subsequent low-rank matrix/tensor approximations.

The HSIs have strong spectral correlation, which is modeled as low-rank property [1, 5, 41] and have also been widely adopted to the HSI denoising. However, only spectral low-rank regularization cannot remove the noise efficiently. One promising improvement is to project the original noisy HSI onto the low-dimensional spectral subspace, and denoise the projected HSI via spatial based methods [10, 29, 46, 47]. Unfortunately, these two-stage methods are significantly influenced by the quality of projection and the efficiency of spatial denoising. All of them fail to capture a clean projection matrix, which makes the restored HSI still be noisy.

To alleviate the aforementioned problems, this paper introduces a unified HSI denoising paradigm to integrate the spatial non-local similarity and global spectral low-rank property simultaneously. We start from the point that the HSI should underlie a low-dimensional spectral subspace, which has been widely accepted in hyperspectral imaging [16, 23], compressive sensing [3, 44], unmixing [2] and dimension reduction [1] tasks. Inspired by this fact, the whole NLFBPGs should also underlie a common low-

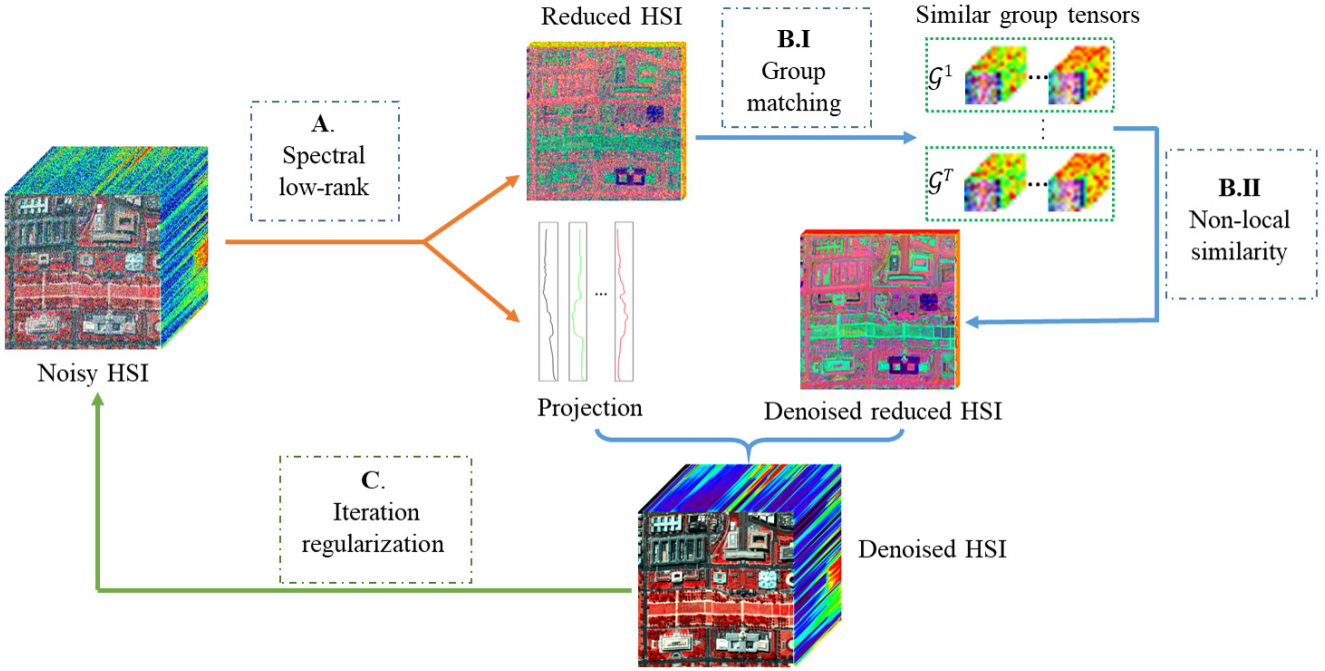


Figure 1. Flowchart of the proposed method. It includes three stages: A. spectral low-rank denoising, B. non-local low-rank denoising and C. iteration regularization. B consists of two steps including group matching and non-local low-rank approximation.

dimensional spectral subspace. Thus, we first learn a global spectral low-rank projection, and subsequently exploit the spatial non-local similarity of projected HSI after the projection. The computational cost of non-local processing in our paradigm will almost keep the same with more spectral bands, and the global spectral low-rank property will also be enhanced. The contributions are summarized as follows:

- We introduce a unified paradigm to exploit the spatial non-local and global spectral low-rank properties simultaneously. We transfer the non-local denoising to the reduced image and improve the computational efficiency against the increase of spectral band number;
- The resulting new model for image denoising is hard to optimize, as it involves with both complex constraint and regularization. We further propose an efficient problem for optimization, which is inspired by alternating minimization;
- Finally, the proposed method is not only the best compared with other state-of-the-art methods in simulated experiment, where Gaussian noise are added manually; but also achieves the most appealing recovered images for real datasets.

Notations We follow the tensor notation in [24], the tensor and matrix are represented as Euler script letters, *i.e.* \mathcal{X} and boldface capital letter, *i.e.* \mathbf{A} , respectively. For a N -order tensor $\mathcal{X} \in \mathbb{R}^{I_1 \times I_2 \times \dots \times I_N}$, the mode- n unfolding operator is denoted as $\mathbf{X}_{(n)} \in \mathbb{R}^{I_n \times I_1 \times \dots \times I_{n-1} \times I_{n+1} \times \dots \times I_N}$. We have $\text{fold}_n(\mathbf{X}_{(n)}) = \mathcal{X}$, in which fold_n is the inverse operator of unfolding operator. The Frobenius norm of \mathcal{X} is

defined by $\|\mathcal{X}\|_F = (\sum_{i_1} \sum_{i_2} \dots \sum_{i_N} x_{i_1 i_2 \dots i_N}^2)^{0.5}$. The mode- n product of a tensor $\mathcal{X} \in \mathbb{R}^{I_1 \times I_2 \times \dots \times I_N}$ and a matrix $\mathbf{A} \in \mathbb{R}^{J_n \times I_n}$ is defined as $\mathcal{Y} = \mathcal{X} \times_n \mathbf{A}$, where $\mathcal{Y} \in \mathbb{R}^{I_1 \times I_2 \times \dots \times J_n}$ and $\mathcal{X} \times_n \mathbf{A} = \text{fold}_n(\mathbf{A} \mathbf{X}_{(n)})$.

2. Related work

Since denoising is an ill-posed problem, proper regulations based on the HSI prior knowledge is necessary [15, 35]. The mainstream of HSI denoising methods can be grouped into two categories: spatial non-local based methods and spectral low-rank based methods.

2.1. Spatial: Non-local similarity

HSIs illustrate the strong spatial non-local similarity. After the non-local low-rank modeling was first introduced to HSI denoising in [28], the flowchart of the non-local based methods become fixed: FBP grouping and low-rank tensor approximation. Almost all the researchers focused on the low-rank tensor modeling of NLFBPGs, such as tucker decomposition [28], sparsity regularized tucker decomposition [36], Laplacian scale mixture low-rank modeling [13], and weighted low-rank tensor recovery [8] to exploit the spatial non-local similarity and spectral low-rank property simultaneously. However, with the increase of spectral number, the computational burden also increases significantly, blocking the application of these methods to the real high-spectrum HSIs.

Chang et.al [9] claimed that the spectral low-rank property of NLFBPGs is weak and proposed a unidirectional low-rank tensor recovery to explore the non-local similarity. It saved much computational burden and achieved the

state-of-the-art performance in the HSI denoising. This reflects the fact that previous non-local low-rank based methods have not yet efficiently utilized the spectral low-rank property. How to balance the importance between spectral low-rank and spatial non-local similarity still remains a problem.

2.2. Spectral: Global low-rank property

The global spectral low-rank property of HSI has been widely accepted and applied to the subsequent applications [1, 5]. As pointed out in [1], the intrinsic dimension of the spectral subspace is far less than the spectral dimension of the original image. By vectorizing each band of the HSI and reshaping the original 3-D HSI into a 2-D matrix, various low-rank approximation methods such as principal components analysis (PCA) [5], robust PCA [11, 37, 41], low-rank matrix factorization [3, 39] have been directly adopted to denoise the HSI. However, these methods only explore the spectral prior of the HSI, ignoring the spatial prior information. Instantly, many conventional spatial regularizers such as total variation [22], low-rank tensor regularization [25, 30] are adopted to explore the spatial prior of HSI combined with spectral low-rank property.

A remedy is a two-stage method combining the spatial regularizer and spectral low-rank property together. This is done by firstly mapping the original HSI into the low-dimensional spectral subspace, and then denoise the mapped image via existing spatial denoising methods, e.g., wavelets [10, 29], BM3D [47] and HOSVD [46]. These two-stage methods provide a new sight to denoise the HSI in the transferred spectral space, which is very fast. However, these methods fail to combine the best of both worlds, and the extracted subspace is still corrupted by the noise.

3. Approaches

In this section, we propose a unified HSI denoising paradigm to integrate spatial non-local similarity and global spectral low-rank property. We first learn a low-dimensional projection and the related reduced image from the noisy HSI. Then the reduced image and the projection are updated by spatial non-local denoising and iteration regularization, respectively. The overview of the proposed paradigm is in Figure 1.

3.1. Unified spatial-spectral paradigm

Assuming that the clean HSI $\mathcal{X} \in \mathbb{R}^{M \times N \times B}$ is corrupted by the additive Gaussian noise \mathcal{N} (with zero mean and variance σ_0^2), then the noisy HSI \mathcal{Y} is generated by

$$\mathcal{Y} = \mathcal{X} + \mathcal{N}. \quad (1)$$

First, to capture the spectral low-rank property in Section 2.2, we are motivated to use a low-rank representation

of the clean HSI \mathcal{X} , *i.e.* $\mathcal{X} = \mathcal{M} \times_3 \mathbf{A}$, where $K \ll B$, $\mathbf{A} \in \mathbb{R}^{B \times K}$ is a projection matrix capturing the common subspace of different spectrum, and $\mathcal{M} \in \mathbb{R}^{M \times N \times K}$ is the reduced image. Second, to utilize the spatial low-rank property, we add a non-local low-rank regularizer $\|\cdot\|_{\text{NL}}$ on the reduced image \mathcal{M} . As a result, the proposed non-local meets global (NGmeet) denoising paradigm is presented as

$$\begin{aligned} \{\mathcal{M}_*, \mathbf{A}_*\} = \arg \min_{\mathcal{M}, \mathbf{A}} & \frac{1}{2} \|\mathcal{Y} \times_3 \mathbf{A}^\top - \mathcal{M}\|_F^2 + \mu \|\mathcal{M}\|_{\text{NL}}, \\ \text{s.t. } & \mathbf{A}^\top \mathbf{A} = \mathbf{I}, \end{aligned} \quad (2)$$

where μ controls the contribution of spatial non-local regularization, the projection matrix \mathbf{A} is required to be orthogonal, and the clean HSI is recovered by $\mathcal{X} = \mathcal{M}_* \times_3 \mathbf{A}_*$.

The objective (2) is very hard to optimize, due to both the orthogonal constraint on \mathbf{A} and complex regularization on \mathcal{M} . An algorithm based on alternating minimization to approximately solve the objective function is proposed in Section 3.2.

Remark 3.1. *The orthogonal constraint $\mathbf{A}^\top \mathbf{A} = \mathbf{I}$ is very important here. First, it encourages the representation held in \mathbf{A} to be more distinguish with each other. This helps to keep noise out of \mathbf{A} and further allows a closed-form solution for computing \mathbf{A} (Section 3.2.1). Besides, it preserves the distribution of noise, which allows us to estimate the remained noise-level in reduced image and reuse the-state-of-art Gaussian based non-local method for spatial denoising (Section 3.2.2).*

However, before going to optimization details, we first look into (2), and see the insights why the proposed method can beat all previous spectral low-rank methods [10, 47].

3.1.1 Necessity of iterative refinement

Recall that, in (2), the first item tries to exploit the spectral low-rank property and decompose the noisy \mathcal{Y} into the coarse spectral low-rank projection \mathbf{A} and reduced image \mathcal{M} . Here, both \mathbf{A} and \mathcal{M} have physical meaning in the field of remote sensing [2]. Specifically, i -th column of \mathbf{A} , denoted as $\mathbf{A}(:, i)$, is regarded as the i -th signature (known as endmember) of HSI, and the corresponding coefficient image $\mathcal{M}(:, :, i)$ is regarded as the abundance map.

Previous methods are mostly two-stage ones, they do not iterative refine the projection matrix they found, *e.g.* FastHyDe [45]. However, we model the spatial and spectral low-rank properties simultaneously, which enables iterative refinement of the projection matrix \mathbf{A} . To demonstrate the necessity of iterative refinement, we calculated the projection \mathbf{A}_1 and reduced image \mathcal{M} from noisy WDC with noise variance 50. The reference \mathbf{A} and \mathcal{M} are from the original clean WDC. Figure 2 presents the comparison on signatures and the corresponding coefficient image before and after our

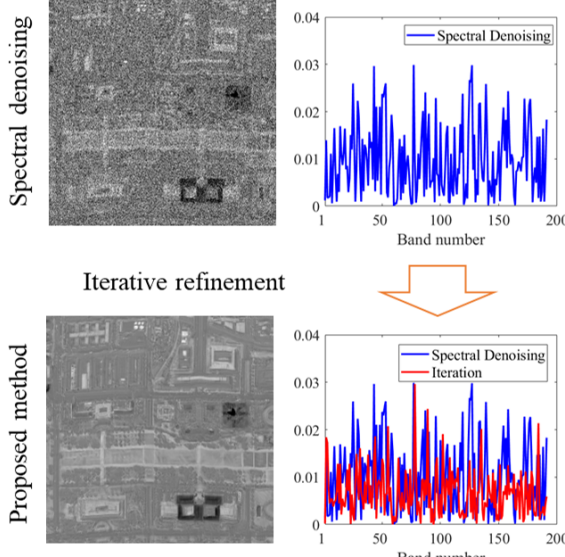


Figure 2. The first row displays the coefficient image $\bar{\mathcal{M}}(:, :, 4)$ and the absolute difference signature between $\mathbf{A}_1(:, 4)$ and the reference. The second row displays the refined coefficient image and the absolute difference signature between refined one and the reference. The test dataset is WDC with noise variance 50.

refinement. From the figure, it can be observed that the projection atom $\mathbf{A}_1(:, 4)$ and reduced image $\bar{\mathcal{M}}$ obtained by the spectral denoising method are still suffering from the noise, while the proposed method can produce much cleaner signatures and coefficient images.

3.2. Efficient optimization

As discussed in Section 3.1, the objective (2) is very hard to optimize. In this section, we are motivated to use alternating minimization for optimization (Algorithm 1). \mathcal{Y}_i , \mathcal{X}_i stand for the input noisy image and output denoised image of the i -th iteration, respectively. As will be shown in the sequel, Algorithm 1 tries to find a closed-form solution for \mathbf{A} (step 3) and reuses the-state-of-art spatial denoising method for computing $\|\cdot\|_{\text{NL}}$ (steps 4-6), which together make the algorithm very efficient. Besides, as \mathbf{A} will be refined during the iteration, iterative regularization [14] is adopted to boost the denoising performance (step 7).

3.2.1 Spectral denoising via \mathbf{A}

In this stage, we identify the projection matrix \mathbf{A} with the given \mathcal{M}_i and \mathcal{Y}_i from (2), which leads to

$$\arg \min_{\mathbf{A}^\top \mathbf{A} = \mathbf{I}} \frac{1}{2} \|\mathcal{Y}_i \times_3 \mathbf{A}^\top - \mathcal{M}_i\|_F^2. \quad (3)$$

However, this problem is hard without simple closed-form solution. Instead, since \mathcal{Y}_i is obtained from iterative regularization, of which the noisy-level is decreased. Thus, we

Algorithm 1 Non-local Meets Global(NGmeet)

Require: Noisy image \mathcal{Y} , noise variance σ_0^2

- 1: $\mathcal{X}_1 = \mathcal{Y}_1 = \mathcal{Y}$, estimating K using HySime [1];
- 2: **for** $i = 1, 2, 3, \dots, \text{iter}$ **do**
- 3: A). *Spectral low-rank denoising*:
Estimate projection matrix \mathbf{A}_i and reduced image $\bar{\mathcal{M}}_i$ via SVD on \mathcal{Y}_i ;
- 4: B). *Non-local reduced image $\bar{\mathcal{M}}_i$ denoising*:
-B.I) Obtain the set of tensors $\{\mathcal{G}^j\}$ for $\bar{\mathcal{M}}_i$ via k -NN search for each reference patch;
- 5: - B.II) Denoise $\{\mathcal{G}^j\}$ via Low-rank approximation and obtain $\{\mathcal{M}_i^j\}$;
- 6: - B.III) Reconstruct the cubes $\{\mathcal{M}_i^j\}$ to image \mathcal{M}_i , and obtain the denoised HSI $\mathcal{X}_i = \mathcal{M}_i \times_3 \mathbf{A}_i$;
- 7: (C). *Iterative regularization*:
 $\mathcal{Y}_{i+1} = \lambda \mathcal{X}_i + (1 - \lambda) \mathcal{Y}$, $K = K + \delta \times i$;
- 8: **end for**
- 9: **return** Denoised image \mathcal{X}_i ;

proposed to relax (3) as

$$\{\bar{\mathcal{M}}_i, \mathbf{A}_i\} = \arg \min_{\mathcal{M}, \mathbf{A}^\top \mathbf{A} = \mathbf{I}} \frac{1}{2} \|\mathcal{Y}_i - \mathcal{M} \times_3 \mathbf{A}\|_F^2, \quad (4)$$

which has the closed-form solution (Proposition 3.1). Thus, only a SVD on the folding matrix of $(\mathcal{Y}_i)_{(3)}$ is required, which can be efficiently computed.

Proposition 3.1. Let $(\mathcal{Y}_i)_{(3)} = \mathbf{U} \mathbf{S} \mathbf{V}^\top$ be the rank- K SVD of $(\mathcal{Y}_i)_{(3)}$. The solution to (4) is given by the close-form as $\mathbf{A}_i = \mathbf{V}$ and $\bar{\mathcal{M}}_i = \text{fold}_3(\mathbf{U} \mathbf{S})$.

3.2.2 Spatial denoising via \mathcal{M}

Note that we have $\bar{\mathcal{M}}_i = \mathcal{Y}_i \times_3 \mathbf{A}_i^\top$ from Section 3.2.1. Using $\bar{\mathcal{M}}_i$ in (2), the objective in this stage becomes:

$$\mathcal{M}_i = \arg \min_{\mathcal{M}} \frac{1}{2} \|\bar{\mathcal{M}}_i - \mathcal{M}\|_F^2 + \mu \|\mathcal{M}\|_{\text{NL}}, \quad (5)$$

where $\|\cdot\|_{\text{NL}}$ is a non-local denoising regularizer. Formulation (5) appears in many denoising models, e.g. WNNM [19]. Specifically, to solve this regularizer, we need to first group similar patches, then denoise each patch group tensors and finally assemble the final estimated \mathcal{M}_i .

However, all these model assume the noise on $\bar{\mathcal{M}}_i$ follow univariate Gaussian distribution. If such assumption fails, the resulting performance can deteriorate significantly. Here, we have the following Proposition 3.2. Therefore, the noise distribution is preserved from \mathcal{Y} to $\bar{\mathcal{M}}_i$, which enables us to use the existing spatial denoising methods. In this paper, we use WNNM [19] to denoise each patch group tensor, as it is widely used and gives the-state-of-art denoising performance.

Proposition 3.2. Assume the noisy HSI \mathcal{Y} is from (1), then the noise on the reduced image $\mathcal{Y} \times_3 \mathbf{P}^\top$, where $\mathbf{P}^\top \mathbf{P} = \mathbf{I}$, still follows Gaussian distribution with zero mean and variance σ_0^2 .

Finally, to use WNNM, we need to estimate the noise level σ_i^2 in $\bar{\mathcal{M}}_i$, whose noise level is changed during the iteration. From Proposition 3.2, we know the noisy level of $\bar{\mathcal{M}}_i$ is the same as \mathcal{Y}_i , thus we propose to estimate it via

$$\sigma_i = \gamma \times \sqrt{|\sigma_0^2 - \text{mean}(\|\mathcal{Y}_i - \mathcal{Y}\|_F^2)|}, \quad (6)$$

where γ is the a scaling factor controlling the re-estimation of noise variance, and $\text{mean}(\cdot)$ stands for the averaging process of the tensor elements. The denoised group tensors are denoted as \mathcal{M}_i^j , which can be directly used to reconstruct the denoised reduced image \mathcal{M}_i . The output denoised image of i -th iteration is $\mathcal{X}_i = \mathcal{M}_i \times_3 \mathbf{A}_i$.

3.2.3 Iterative refinement

Iteration regularization has been widely used to boost the denoising performance [9, 14, 19, 36]. Here we also introduce the it into our model (Algorithm 1) to refine the noisy projection \mathbf{A}_i . As shown in (4), the projection is significantly influenced by the noise intensity of input noisy image \mathcal{Y}_i . Hence we update the next input noisy image as

$$\mathcal{Y}_{i+1} = \lambda \mathcal{X}_i + (1 - \lambda) \mathcal{Y},$$

where λ is to trade-off the denoised image \mathcal{X}_i and original noisy image \mathcal{Y} . The estimation of \mathbf{A}_i can benefit from the lower noise variance of the input \mathcal{Y}_{i+1} .

Besides, K is also updated with the iteration. We initialize K by HySime [1]. When the noisy image \mathcal{Y} is corrupted by heavy noise, the estimated K will be small. Fortunately, the larger singular values obtained from the noisy image are less contaminated by the noise, and help to keep noise out of the reduced image. With the iteration, We increase K by

$$K = K + \delta \times i, \quad (7)$$

where δ is a constant value. Therefore, \mathbf{A}_{i+1} has the ability to capture more useful information with more iterations.

3.3. Complexity analysis

Following the procedure of Algorithm 1, the main time complexity of each iteration includes stage A-SVD ($\mathcal{O}(MNB^2)$), stage B.non-local low-rank denoising of each \mathcal{G}^j $\mathcal{O}(Tn^2Kp^2)$. Table 1 presents the time complexity comparison between NGmeet and other non-local HSI denoising method. LLRT and KBR only need stage B to complete the denoising. As can be seen, the proposed NGmeet costs additional $\mathcal{O}(MNB^2)$ complexity in stage A, however, will be at least B/K times faster in stage B.

Table 1. Complexity comparison of each iteration between proposed NGmeet and state-of-the-arts non-local based methods. $\mathcal{G}_i \in \mathbb{R}^{n \times n \times K \times p}$, where n is the size of each patch and p is the number of similar patches. T is the number of $\{\mathcal{G}^j\}$ and T_o is the inner iteration of KBR.

	stage A	stage B
NGmeet	$\mathcal{O}(MNB^2)$	$\mathcal{O}(Tn^2Kp^2)$
LLRT	—	$\mathcal{O}(Tn^2Bp^2)$
KBR	—	$\mathcal{O}(TT_0(n^2Bp(n^2 + B + p) + n^6 + B^3 + p^3))$

4. Experiments

In this section, we present the simulated and real data experimental results of different methods, companied with the computational efficiency and parameter analysis of the proposed NGmeet. The experiments are programmed in Matlab with CPU Core i7-7820HK 64G memory.

4.1. Simulated experiments

Setup. One multi-spectral image (MSI) CAVE ¹, and two HSI images, *i.e.* PaC ² and WDC ³ datasets are used (Table 3). These images have been widely used for a simulated study [9, 21, 28, 36, 47]. Following the settings in [9, 28], additive Gaussian noise with noise variance σ_0^2 are added to the MSIs/HSIs with σ_0^2 varies from 10, 30, 50 to 100. Before denoising, the whole HSIs are normalized to [0, 255].

The following methods are used for the comparison: *spectral low-rank methods*, *i.e.* LRTA [30] ⁴, LRTV [22] ⁵, MTSNMF [39] ⁶, NAILRMA [21] PARAFAC [26] and FastHyDe [47] ⁷; *spatial low-rank methods*, *i.e.* TDL [28] KBR [36] ⁸, LLRT [9] ⁹; and finally NGmeet (Algorithm 1), which combines the best of above two fields. Hyperparameters of all compared methods are set based on authors' codes or suggestions in the paper. The value of spectral dimension K is the most import parameter, which is initialized by HySime [1] and updated via (7). Parameter μ is used to control the contribution of non-local regularization, and γ is a scaling factor controlling the re-estimation of noise variance [14]. We empirically set $\mu = 1$, $\lambda = 0.9$ and $\gamma = 0.5$ as introduced in [9], and $\delta = 2$ in the whole experiments.

To thoroughly evaluate the performance of different methods, the peak signal-to-noise ratio (PSNR) index, the structural similarity (SSIM) [34] index and the spectral angle mean (SAM) [9, 22] index were adopted to give a quan-

¹<http://www1.cs.columbia.edu/CAVE/databases/>

²<http://www.ehu.eus/ccwintco/index.php/>

³<https://engineering.purdue.edu/~biehl/MultiSpec/hyperspectral>

⁴<https://www.sandia.gov/tgkolda/TensorToolbox/>

⁵<https://sites.google.com/site/rshewei/home>

⁶<https://www.cs.zju.edu.cn/people/qianynt/>

⁷<http://www.lx.it.pt/~bioucas/>

⁸<http://gr.xjtu.edu.cn/web/dymeng/>

⁹<http://www.escience.cn/people/changyi/>

Table 2. Quantitative comparison of different algorithms under various noise levels. The PSNR is in dB, and best results is in bold.

Image	σ	Index	spectral low-rank methods						spatial low-rank methods			NG-meet
			LRTA	LRTV	MTS-NMF	NAIL-RMA	PARA-FAC	Fast-HyDe	TDL	KBR	LLRT	
CAVE	10	PSNR	44.12	41.47	44.27	28.51	38.01	46.72	45.58	46.20	47.14	47.87
		SSIM	0.969	0.949	0.972	0.941	0.921	0.985	0.983	0.980	0.989	0.990
		SAM	7.90	16.54	8.49	14.52	13.86	6.62	6.07	8.94	4.65	4.72
	30	PSNR	38.68	35.32	37.18	35.11	37.58	41.21	39.67	41.52	42.53	43.11
		SSIM	0.913	0.818	0.855	0.775	0.888	0.945	0.942	0.942	0.974	0.972
		SAM	12.86	33.32	14.97	32.43	17.37	14.06	12.54	19.43	8.23	7.46
	50	PSNR	35.49	32.27	33.40	32.11	30.06	38.05	36.51	39.41	40.09	40.45
		SSIM	0.858	0.719	0.730	0.638	0.571	0.889	0.888	0.922	0.950	0.951
		SAM	16.53	43.65	19.06	22.85	38.35	20.08	18.23	21.31	11.48	9.80
	100	PSNR	31.21	27.97	27.96	27.90	24.29	33.41	31.90	33.78	36.25	37.21
		SSIM	0.735	0.529	0.493	0.453	0.256	0.746	0.734	0.851	0.910	0.927
		SAM	22.67	54.85	26.33	55.66	51.83	30.72	28.51	26.41	18.17	16.23
PaC	10	PSNR	38.49	38.71	40.64	41.46	33.39	42.220	41.46	40.09	41.95	43.17
		SSIM	0.975	0.979	0.988	0.987	0.866	0.990	0.988	0.984	0.989	0.992
		SAM	4.90	3.29	2.76	3.46	9.05	2.99	3.06	2.86	2.75	2.61
	30	PSNR	32.07	32.76	35.45	34.17	30.92	35.98	34.43	34.39	35.04	36.97
		SSIM	0.908	0.920	0.958	0.941	0.845	0.962	0.949	0.947	0.957	0.971
		SAM	7.88	5.76	4.17	6.54	9.28	5.09	5.11	4.28	4.86	4.30
	50	PSNR	29.11	29.45	32.51	30.71	29.24	33.32	31.31	31.05	32.00	34.29
		SSIM	0.836	0.850	0.921	0.886	0.846	0.936	0.904	0.892	0.918	0.948
		SAM	9.20	8.60	5.50	8.83	11.40	6.55	6.14	5.40	6.55	5.18
	100	PSNR	25.13	26.22	28.17	25.76	23.68	29.90	27.49	27.80	28.63	30.61
		SSIM	0.655	0.729	0.808	0.728	0.598	0.873	0.789	0.793	0.833	0.890
		SAM	10.17	12.76	8.40	12.93	20.22	8.68	7.67	6.95	7.68	6.86
WDC	10	PSNR	38.94	36.64	37.26	42.57	32.38	43.06	41.83	40.58	41.89	43.72
		SSIM	0.974	0.968	0.975	0.989	0.914	0.991	0.989	0.986	0.990	0.993
		SAM	5.602	4.653	4.429	3.637	8.087	3.070	3.680	3.090	3.700	2.830
	30	PSNR	32.91	32.42	34.65	35.87	31.56	37.390	34.84	34.75	36.30	37.90
		SSIM	0.917	0.909	0.953	0.958	0.898	0.971	0.953	0.951	0.967	0.975
		SAM	8.331	5.991	5.557	7.011	9.009	5.140	6.400	5.240	5.460	4.640
	50	PSNR	30.35	30.12	32.49	32.56	29.49	34.61	31.89	31.61	33.48	35.14
		SSIM	0.864	0.849	0.922	0.919	0.837	0.948	0.910	0.900	0.938	0.955
		SAM	9.43	7.09	6.71	9.22	13.64	6.57	7.94	6.63	6.43	5.83
	100	PSNR	26.84	27.23	28.94	27.85	23.01	31.05	27.66	28.23	29.88	31.45
		SSIM	0.734	0.740	0.830	0.805	0.550	0.894	0.781	0.789	0.861	0.903
		SAM	11.33	9.47	9.44	13.27	25.46	8.91	10.15	9.12	7.99	7.86

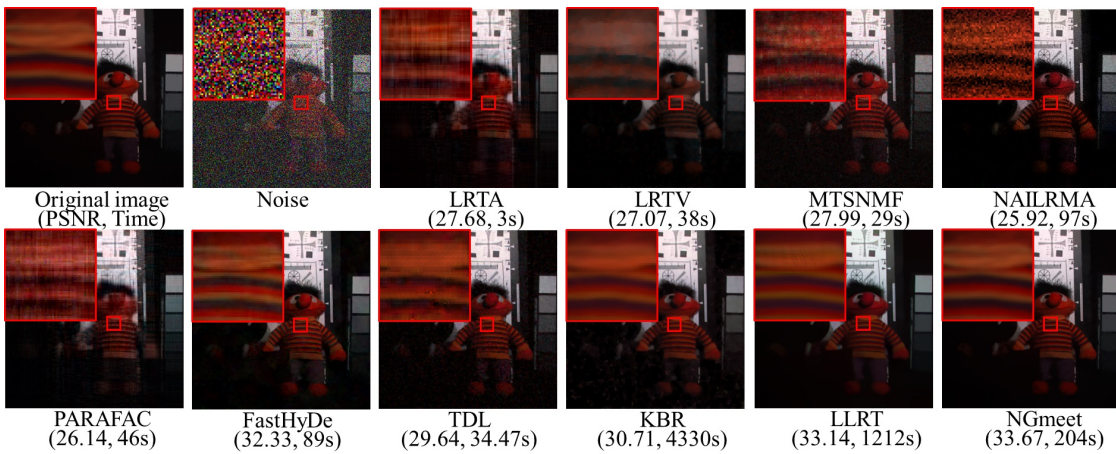


Figure 3. Denoising results on the CAVE-toy image with the noise variance 100. The color image is composed of bands 31, 11, and 6 for the red, green, and blue channels, respectively.

titative assessment. The SAM index is to measure the mean spectrum degree between the original HSI and the restored HSI. The lower value of SAM means the higher similarity

between original image and the denoised image.

Quantitative comparison. For each noise level setting, we calculate evaluation values of all the images from each

Table 3. Hyper-spectral images used for simulated experiments.

	CAVE	PaC	WDC
image size	512×512	256×256	256×256
number of bands	31	89	192

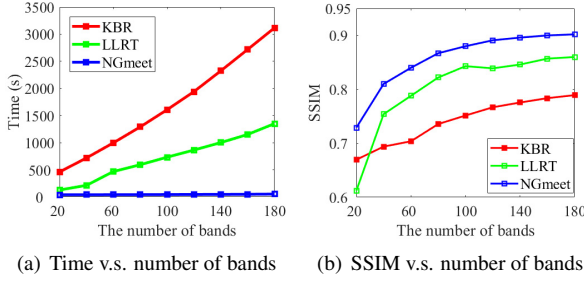


Figure 4. The computational time and SSIM values of different numbers of bands. WDC is used and noise variance is 100.

dataset, as presented in Table 2. It can be easily observed that the proposed NGmeet method achieved the best results almost in all cases. Another interesting observation is that the non-local based method LLRT can achieve better results than FastHyDe, the best result of spectral low-rank methods, but it dose the opposite in the hyperspectral image cases. This phenomenon conforms the advantage of NL low-rank property in the MSI processing and the spectral low-rank property in the HSI processing.

Visual comparison. To further demonstrate the efficiency of the proposed method, Figure 3 shows the color images of CAVE-toy (composed of bands 31, 11 and 6 [21]) before and after denoising. The results of PaC and WDC can be found in the supplementary material. The PSNR values and the computational time of each methods are marked under the denoised images. It can be observed that FastHyDe, LLRT and NGmeet have huge advantage over the rest comparison methods. From the enlarged area, the results of FastHyDe LLRT produced some artifacts. Thus, our method NGmeet can produce the best visual quality.

Table 4. Average running time (in seconds) of each stage for the non-local low-rank based methods. stage A: spectral projection; stage B: spatial non-local low-rank denoising.

Time (seconds)	KBR		LLRT		NGmeet
	stage B	stage B	stage B	stage A	
CAVE	4330	1212	3	201	204
PaC	828	488	2	37	39
WDC	3570	1573	3	45	48

Computational efficiency. In this section, we will illustrate that in our denoising paradigm, the computational efficiency of the non-local denoising procedure will get rid of the huge spectral dimension. Compared to the previous non-local denoising methods, *i.e.* KBR [36] and LLRT [9], the proposed NGmeet includes additional stage A. Table 4 presents the computational time of different stages of the three methods. From Table 1 and 4, we can conclude that NGmeet spends little time to project the original HSI onto a reduced image (stage A), however, earning huge advantage

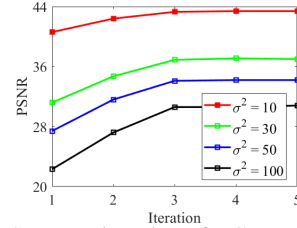


Figure 5. PSNR v.s. iteration of NGmeet. WDC is used.

in stage B including group matching step and non-local denoising.

Figure 4 displays the computational time and SSIM values of the proposed NGmeet, KBR [36] and LLRT [9], with the increase of spectral number. As illustrated, even though the performances of KBR and LLRT increase with the increase of spectral number, the computational time also increases linearly. Our method can achieve the best performance, meanwhile, the computational time is nearly unchanged with the increase of spectral number.

Convergence. To show the convergence of proposed NGmeet, Figure 5 presents the PSNR values with the increase of iteration, on the WDC dataset. From the figure, it can be observed that our method can converge to stable PSNR values very fast at different noise level.

4.2. Real Data Experiments

Setup. Here, AVIRIS Indian Pines HSI¹⁰ and HYDICE Urban image¹¹ are adopted in the real experiments (Table 5). The noisy HSIs are also scaled to the range [0 255], and the parameters involved in the proposed methods are set as the same in the simulated experiments. In addition, multiple regression theory-based approach [1] is adopted to estimate the initial noise variance of each HSI bands.

Table 5. Hyperspectral images used for real data experiments.

	Urban	Indian Pines
image size	200×200	145×145
number of bands	210	220

Visual comparison. Since reference clean images are missing, we just present the real Indian Pines and Urban images before and after denoising in figures 6 and 7. It can be obviously observed that the results produced by the proposed NGmeet can remove the noise and keep the spectral details simultaneously. LRTV can produce the most smooth results. However, the color of the denoised result changes a lot, indicating the loss of spectral information. The denoised results of FastHyDe and LLRT still contain stripes as presented in Figure 6. To sum up, although the proposed NGmeet is designed in the Gaussian noise assumption, it can also achieve the best results for real datasets.

¹⁰<https://engineering.purdue.edu/~biehl/MultiSpec/>

¹¹<http://www.tec.army.mil/hypercube>

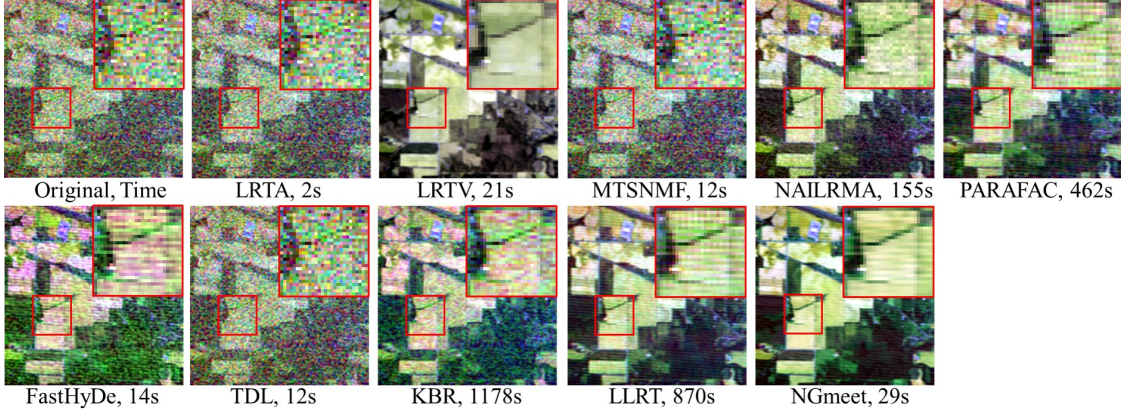


Figure 6. Real data experimental results on the Indian Pines dataset. The color image is composed of bands 219, 109 and 1.

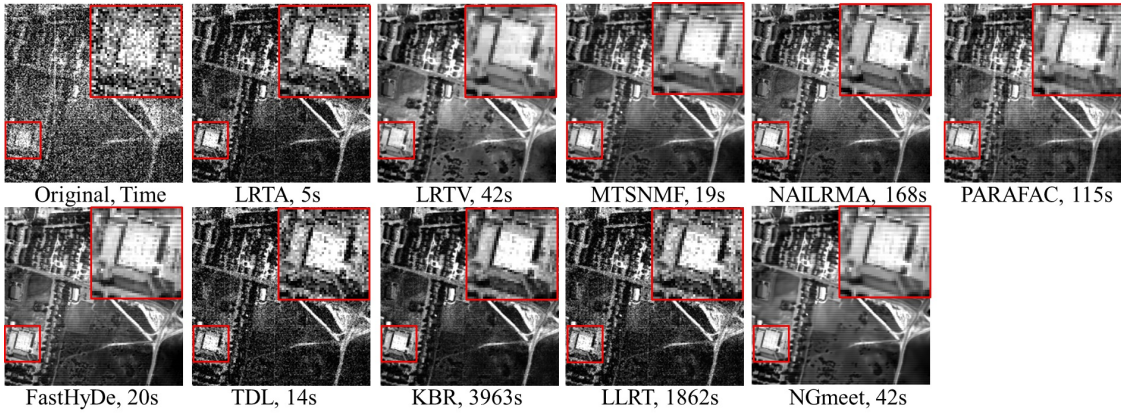


Figure 7. Real data experimental results on the Urban dataset of band 207.

4.3. Parameter analysis

K is the key parameter to integrate the spatial and spectral information. Figure 8 presents the PSNR values achieved by NGmeet with different initialization of K with δ being 0. PaC images was chosen as the test image, and the noise variance σ_0^2 changes from 10, 30, 50 to 100. K is initialized by HySime [1] as 7, 6, 6, 5 for different noise variance cases, respectively. It confirms that the initialization of K is reliable.

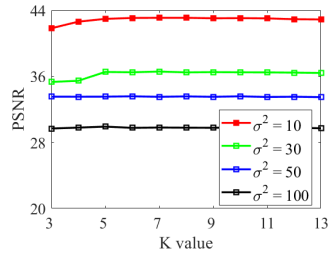


Figure 8. PSNR values achieved by the proposed methods with different parameter K with $\delta = 0$ on the PaC dataset.

Table 6 presents the influence of different σ_0^2 values with K being initialized by HySime [1]. It can be observed that,

the updating strategy of K can improve the performance, and the selection of δ is robust.

Table 6. The influence of different δ for NGmeet.

PSNR(dB)	$\sigma_0^2 = 10$	$\sigma_0^2 = 30$	$\sigma_0^2 = 50$	$\sigma_0^2 = 100$
$\delta = 0$	43.09	36.49	33.54	29.91
$\delta = 1$	43.52	36.96	34.23	30.56
$\delta = 2$	43.43	37.02	34.21	30.83
$\delta = 3$	43.42	37.11	34.42	30.45

5. Conclusion

In this paper, we provide a new perspective to integrate the spatial non-local similarity and global spectral low-rank property, which are explored by low-dimensional projection and reduced image denoising, respectively. We have also proposed an alternating minimization method with iteration strategy to solve the optimization of the proposed GNmeet method. The superiority of our method are confirmed by the simulated and real dataset experiments. In our unified spatial-spectral paradigm, the usage of WNNM [19] is not a must. In future, we plan to adopt Convolutional Neural Network [7, 42] to explore non-local similarity.

References

- [1] J. M. Bioucas-Dias and J. M. Nascimento. Hyperspectral subspace identification. *IEEE Trans. Geosci. Remote Sens.*, 46(8):2435–2445, Aug. 2008. [1](#), [3](#), [4](#), [5](#), [7](#), [8](#)
- [2] J. M. Bioucas-Dias, A. Plaza, N. Dobigeon, M. Parente, Q. Du, P. Gader, and J. Chanussot. Hyperspectral unmixing overview: Geometrical, statistical, and sparse regression-based approaches. *IEEE J. Sel. Topics Appl. Earth Observ. Remote Sens.*, 5(2):354–379, Apr. 2012. [1](#), [3](#)
- [3] X. Cao, Q. Zhao, D. Meng, Y. Chen, and Z. Xu. Robust low-rank matrix factorization under general mixture noise distributions. *IEEE Trans. on Image Process.*, 25(10):4677–4690, Oct 2016. [1](#), [3](#)
- [4] A. Chakrabarti and T. Zickler. Statistics of real-world hyperspectral images. In *CVPR*, pages 193–200, June 2011. [1](#)
- [5] C.-I. Chang and Q. Du. Interference and noise-adjusted principal components analysis. *IEEE Trans. Geosci. Remote Sens.*, 37(5):2387–2396, Sep. 1999. [1](#), [3](#)
- [6] Y. Chang, L. Yan, H. Fang, and C. Luo. Anisotropic spectral-spatial total variation model for multispectral remote sensing image despeckling. *IEEE Trans. on Image Process.*, 24(6):1852–1866, Jun. 2015. [1](#)
- [7] Y. Chang, L. Yan, H. Fang, S. Zhong, and W. Liao. Hsi-denet: Hyperspectral image restoration via convolutional neural network. *IEEE Trans. Geosci. Remote Sens.*, pages 1–16, 2018. [8](#), [11](#)
- [8] Y. Chang, L. Yan, H. Fang, S. Zhong, and Z. Zhang. Weighted low-rank tensor recovery for hyperspectral image restoration. *arXiv preprint arXiv:1709.00192*, 2017. [2](#)
- [9] Y. Chang, L. Yan, and S. Zhong. Hyper-laplacian regularized unidirectional low-rank tensor recovery for multispectral image denoising. In *CVPR*, pages 4260–4268, 2017. [1](#), [2](#), [5](#), [7](#)
- [10] G. Chen and S.-E. Qian. Denoising of hyperspectral imagery using principal component analysis and wavelet shrinkage. *IEEE Trans. Geosci. Remote Sens.*, 49(3):973–980, Mar. 2011. [1](#), [3](#)
- [11] Y. Chen, Y. Guo, Y. Wang, D. Wang, C. Peng, and G. He. Denoising of hyperspectral images using non-convex low rank matrix approximation. *IEEE Trans. Geosci. Remote Sens.*, 55(9):5366–5380, Jun. 2017. [3](#)
- [12] R. Dian, L. Fang, and S. Li. Hyperspectral image super-resolution via non-local sparse tensor factorization. In *2017 IEEE Conference on Computer Vision and Pattern Recognition (CVPR)*, pages 3862–3871, July 2017. [1](#)
- [13] W. Dong, G. Li, G. Shi, X. Li, and Y. Ma. Decomposable nonlocal tensor dictionary learning for multispectral image denoising. In *ICCV*, pages 442–449, 2015. [1](#), [2](#)
- [14] W. Dong, G. Shi, and X. Li. Nonlocal image restoration with bilateral variance estimation: a low-rank approach. *IEEE Trans. on Image Process.*, 22(2):700–711, 2013. [4](#), [5](#)
- [15] Y. Fu, A. Lam, I. Sato, and Y. Sato. Adaptive spatial-spectral dictionary learning for hyperspectral image restoration. *International Journal of Computer Vision*, 122(2):228–245, 2017. [2](#)
- [16] Y. Fu, Y. Zheng, I. Sato, and Y. Sato. Exploiting spectral-spatial correlation for coded hyperspectral image restoration. In *CVPR*, pages 3727–3736, June 2016. [1](#)
- [17] C. Gendrin, Y. Roggo, and C. Collet. Pharmaceutical applications of vibrational chemical imaging and chemometrics: A review. *J. Pharm. Biomed. Anal.*, 48(3):533 – 553, Nov. 2008. [1](#)
- [18] R. O. Green, M. L. Eastwood, C. M. Sarture, T. G. Chrien, M. Aronsson, B. J. Chippendale, J. A. Faust, B. E. Pavri, C. J. Chovit, M. Solis, M. R. Olah, and O. Williams. Imaging spectroscopy and the airborne visible/infrared imaging spectrometer (aviris). *Remote Sens. Environ.*, 65(3):227–248, Sep. 1998. [1](#)
- [19] S. Gu, L. Zhang, W. Zuo, and X. Feng. Weighted nuclear norm minimization with application to image denoising. In *CVPR*, pages 2862–2869, 2014. [4](#), [5](#), [8](#)
- [20] B. F. Guolan Lu. Medical hyperspectral imaging: a review. *Journal of Biomedical Optics*, 19:19 – 19 – 24, 2014. [1](#)
- [21] W. He, H. Zhang, L. Zhang, and H. Shen. Hyperspectral image denoising via noise-adjusted iterative low-rank matrix approximation. *IEEE J. Sel. Topics Appl. Earth Observ. Remote Sens.*, 8(6):3050–3061, 2015. [5](#), [7](#), [11](#)
- [22] W. He, H. Zhang, L. Zhang, and H. Shen. Total-variation-regularized low-rank matrix factorization for hyperspectral image restoration. *IEEE Trans. Geosci. Remote Sens.*, 54(1):178–188, Jan. 2016. [3](#), [5](#)
- [23] R. Kawakami, Y. Matsushita, J. Wright, M. Ben-Ezra, Y. W. Tai, and K. Ikeuchi. High-resolution hyperspectral imaging via matrix factorization. In *CVPR 2011*, pages 2329–2336, June 2011. [1](#)
- [24] T. Kolda and B. Bader. Tensor decompositions and applications. *SIAM Review*, 51(3):455–500, 2009. [2](#)
- [25] C. Li, Y. Ma, J. Huang, X. Mei, and J. Ma. Hyperspectral image denoising using the robust low-rank tensor recovery. *JOSA A*, 32(9):1604–1612, 2015. [3](#)

[26] X. Liu, S. Bourennane, and C. Fossati. Denoising of hyperspectral images using the parafac model and statistical performance analysis. *IEEE Trans. Geosci. Remote Sens.*, 50(10):3717–3724, 2012. 5

[27] Z. Pan, G. Healey, M. Prasad, and B. Tromberg. Face recognition in hyperspectral images. *IEEE Trans. Pattern Anal. Mach. Intell.*, 25(12):1552–1560, Dec 2003. 1

[28] Y. Peng, D. Meng, Z. Xu, C. Gao, Y. Yang, and B. Zhang. Decomposable nonlocal tensor dictionary learning for multispectral image denoising. In *CVPR*, pages 2949–2956, 2014. 1, 2, 5

[29] B. Rasti, J. R. Sveinsson, M. O. Ulfarsson, and J. A. Benediktsson. Hyperspectral image denoising using first order spectral roughness penalty in wavelet domain. *IEEE J. Sel. Topics Appl. Earth Observ. Remote Sens.*, 7(6):2458–2467, Jun. 2014. 1, 3

[30] N. Renard, S. Bourennane, and J. Blanc-Talon. Denoising and dimensionality reduction using multilinear tools for hyperspectral images. *IEEE Geosci. Remote Sens. Lett.*, 5(2):138–142, Apr. 2008. 3, 5

[31] G. A. Shaw and H.-h. K. Burke. Spectral imaging for remote sensing. *Lincoln Laboratory Journal*, 14(1):3–28, 2003. 1

[32] D. W. Stein, S. G. Beaven, L. E. Hoff, E. M. Winter, A. P. Schaum, and A. D. Stocker. Anomaly detection from hyperspectral imagery. *IEEE Signal Process Mag.*, 19(1):58–69, 2002. 1

[33] M. Uzair, A. Mahmood, and A. Mian. Hyperspectral face recognition with spatirospectral information fusion and pls regression. *IEEE Trans. on Image Process.*, 24(3):1127–1137, March 2015. 1

[34] Z. Wang, A. C. Bovik, H. R. Sheikh, and E. P. Simoncelli. Image quality assessment: from error visibility to structural similarity. *IEEE Trans. on Image Process.*, 13(4):600–612, 2004. 5

[35] W. Wei, L. Zhang, C. Tian, A. Plaza, and Y. Zhang. Structured sparse coding-based hyperspectral imagery denoising with intracluster filtering. *IEEE Trans. Geosci. Remote Sens.*, 55(12):6860–6876, 2017. 2

[36] Q. Xie, Q. Zhao, D. Meng, and Z. Xu. Kronecker-basis-representation based tensor sparsity and its applications to tensor recovery. *IEEE Trans. Pattern Anal. Mach. Intell.*, 40(8):1888–1902, 2018. 1, 2, 5, 7

[37] Y. Xie, Y. Qu, D. Tao, W. Wu, Q. Yuan, W. Zhang, et al. Hyperspectral image restoration via iteratively regularized weighted schatten p-norm minimization. *IEEE Trans. Geosci. Remote Sens.*, 54(8):4642–4659, Aug. 2016. 3

[38] F. Yasuma, T. Mitsunaga, D. Iso, and S. K. Naray. Generalized assorted pixel camera: Postcapture control of resolution, dynamic range, and spectrum. *IEEE Trans. on Image Process.*, 19(9):2241–2253, Sept 2010. 1

[39] M. Ye, Y. Qian, and J. Zhou. Multitask sparse non-negative matrix factorization for joint spectral-spatial hyperspectral imagery denoising. *IEEE Trans. Geosci. Remote Sens.*, 53(5):2621–2639, May 2015. 3, 5

[40] Q. Yuan, Q. Zhang, J. Li, H. Shen, and L. Zhang. Hyperspectral image denoising employing a spatial-spectral deep residual convolutional neural network. *IEEE Trans. Geosci. Remote Sens.*, pages 1–14, 2018. 11

[41] H. Zhang, W. He, L. Zhang, H. Shen, and Q. Yuan. Hyperspectral image restoration using low-rank matrix recovery. *IEEE Trans. Geosci. Remote Sens.*, 52(8):4729–4743, Aug. 2014. 1, 3

[42] K. Zhang, W. Zuo, S. Gu, and L. Zhang. Learning deep cnn denoiser prior for image restoration. In *CVPR*, volume 2, 2017. 8

[43] L. Zhang, W. Wei, Y. Zhang, C. Shen, A. van den Hengel, and Q. Shi. Cluster sparsity field for hyperspectral imagery denoising. In *ECCV*, pages 631–647, 2016. 1

[44] L. Zhang, W. Wei, Y. Zhang, C. Tian, and F. Li. Reweighted laplace prior based hyperspectral compressive sensing for unknown sparsity. In *CVPR*, June 2015. 1

[45] X. Zhang, X. Yuan, and L. Carin. Nonlocal low-rank tensor factor analysis for image restoration. In *CVPR*, pages 8232–8241, 2018. 1, 3

[46] L. Zhuang and J. M. Bioucas-Dias. Hyperspectral image denoising based on global and non-local low-rank factorizations. In *ICIP*, pages 1900–1904. IEEE, 2017. 1, 3

[47] L. Zhuang and J. M. Bioucas-Dias. Fast hyperspectral image denoising and inpainting based on low-rank and sparse representations. *IEEE J. Sel. Topics Appl. Earth Observ. Remote Sens.*, 11(3):730–742, Mar. 2018. 1, 3, 5

A. Proof

A.1. Proposition 3.1

Proof. Note that the objective can be expressed as:

$$\min_{\mathbf{M}_{(3)}, \mathbf{A}^\top \mathbf{A} = \mathbf{I}} \frac{1}{2} \|(\mathbf{Y}_i)_{(3)} - \mathbf{M}_{(3)} \mathbf{A}\|_F^2,$$

which is equal to find the best K -rand approximation of $(\mathbf{Y}_i)_{(3)}$. Thus, let rank- K SVD of $(\mathbf{Y}_i)_{(3)}$ be \mathbf{U} , \mathbf{S} and \mathbf{V} , the closed-form solution of (4) is given by $\mathbf{A}_i = \mathbf{V}$ and $\bar{\mathcal{M}}_i = \text{fold}_3(\mathbf{U}\mathbf{S})$. \square

A.2. Proposition 3.2

Proof. Since $\mathcal{Y} = \mathcal{X} + \mathcal{N}$, then

$$\mathcal{Y} \times_3 \mathbf{P} = \mathcal{X} \times_3 \mathbf{P} + \mathcal{N} \times_3 \mathbf{P}, \quad (8)$$

where the noise is given by $\mathcal{N} \times_3 \mathbf{P}$. Note that

$$\text{mean}[\mathcal{N} \times_3 \mathbf{P}] = \mathbf{0}. \quad (9)$$

Thus, the mean of the noise is zero. Let \mathbf{a} be a column in $\mathbf{N}_{(3)}$, then one column \mathbf{b} in $(\mathcal{N} \times_3 \mathbf{P})_3$ can be expressed as

$$\mathbf{b} = \mathbf{P}\mathbf{a}. \quad (10)$$

Follow the definition of variance, we have

$$\begin{aligned} \text{var}[\mathbf{b}] &= \text{mean}[(\mathbf{b} - \text{mean}[\mathbf{b}])^2] \\ &= \text{mean}[\mathbf{b}\mathbf{b}^\top] \\ &= \text{mean}[\mathbf{a}^\top \mathbf{P}^\top \mathbf{P}\mathbf{a}] \\ &= \text{mean}[\mathbf{a}^\top \mathbf{a}] = \sigma_0 \mathbf{I}. \end{aligned}$$

Thus, we obtain the proposition. \square

B. Extra Experiments Results

Figure 9 and 10 show the color images of PaU [21] (composed of bands 80, 34 and 9) and WDC (composed of bands 190, 60 and 27) before and after denoising.

C. Deep Networks

Very recently deep learning based HSI denoising methods, *i.e.* HSID-CNN [40] and HSI-DeNet [7] have been proposed. We didn't compare the proposed NGmeet with these two methods, since the related codes are not public available. However, from the cross-over experimental report between our method and the two deep learning based methods, we found that our method performs much better than HSID-CNN [40] in the WDC data case with Gaussian noise. HSI-DeNet [7] didn't report the Gaussian noise removal of CAVE dataset. However, if we regard LLRT as a baseline, the improvement of our NGmeet compared to LLRT is a bit higher than that of HSI-DeNet [7]. These evidences prove the validity of our method compared to the state-of-the-art deep learning based methods.

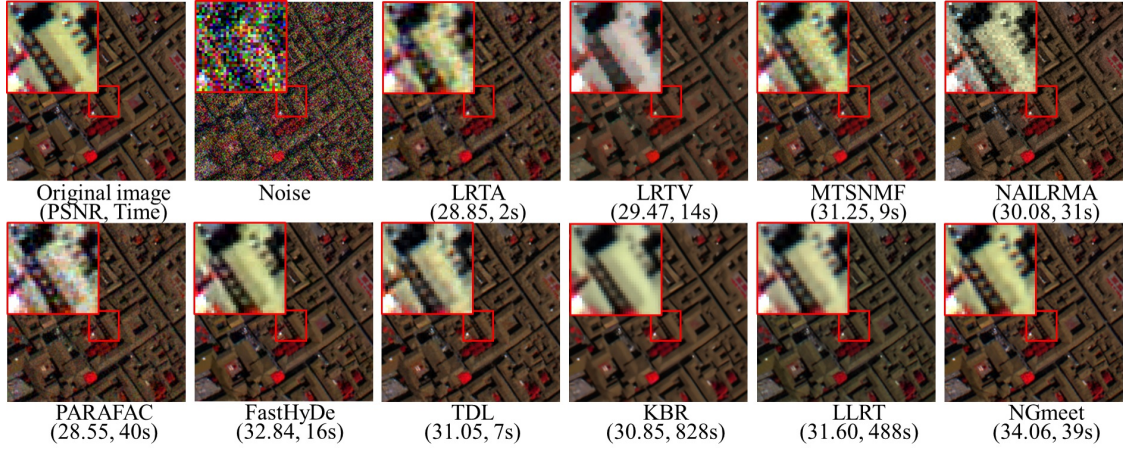


Figure 9. Denoising results on the PaU image with the noise variance 50. The color image is composed of bands 80, 34, and 9 for the red, green, and blue channels, respectively.

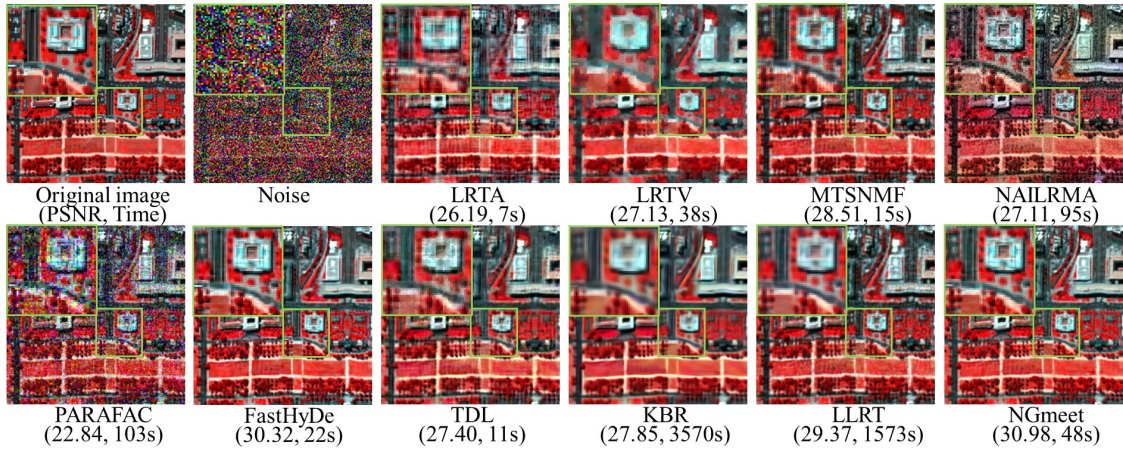


Figure 10. Denoising results on the WDC image with the noise variance 100. The color image is composed of bands 190, 60 and 27 for the red, green, and blue channels, respectively.